Available online at www.sciencedirect.com

ScienceDirect

Solar Energy 124 (2016) 163–176

SOLAR ENERGY

www.elsevier.com/locate/solener

Solar molten salt heated membrane reformer for natural gas upgrading and hydrogen generation: A CFD model

Syed A.M. Said [a,*,1], David S.A. Simakov [b,*,1], Mohammed Waseeuddin [a], Yuriy Román-Leshkov [c,*]

[a] Department of Mechanical Engineering, King Fahd University of Petroleum & Minerals, Dhahran 31261, Saudi Arabia
[b] Department of Chemical Engineering, University of Waterloo, Waterloo, ON N2L 3G1, Canada
[c] Department of Chemical Engineering, Massachusetts Institute of Technology, Cambridge, MA 02139, USA

Received 20 August 2015; received in revised form 23 November 2015; accepted 23 November 2015

Communicated by: Associate Editor Michael EPSTEIN

Abstract

Parabolic trough solar collectors can be used to drive endothermic reactions, such as methane reforming, while using molten salts as a heat transfer fluid. However, linear focus concentrators can only provide temperatures under 600 °C, resulting in CH_4 conversions well below 50%. The equilibrium can be shifted toward much higher conversions if H_2 is continuously removed from the reaction mixture via a H_2-selective membrane, while simultaneously generating a high-purity H_2 stream. In this study, a tube-and-shell, molten salt-heated packed bed membrane reformer (Ni/Al_2O_3 catalyst, 5 μm supported Pd film membrane) is analyzed numerically using computational fluid dynamics and non-isothermal formulation. The effects of molten salt supply rate and reforming feed flow rate on the reformer performance, which is evaluated in terms of CH_4 conversion, H_2 recovery, and selectivity to CO, are investigated. Depending on operating parameters, significant temperature and concentration gradients may form in both axial and radial directions. These gradients can be prevented by adjusting feed rates in the reforming and molten salt compartments. For the optimized case, CH_4 conversion of 99% and H_2 recovery of 87% are predicted for the molten salt feed temperature of 600 °C and reforming feed space velocity of 5000 h^{-1}, which corresponds to a power density of 1.9 kW/L and a fuel heating value upgrade of 40%. A preliminary techno-economic evaluation is provided.

Keywords: Parabolic trough; Membrane reformer; Methane; Hydrogen

1. Introduction

The intensive use of fossil fuels for power generation and transportation leads to large emissions of carbon dioxide that contributes to global warming (Keller and Warming, 2007). Alternative sources of energy, preferably renewable in nature, are clearly required. Solar radiation is an abundant and environmentally benign source of energy. An effective way to capture solar energy is to convert it to chemical energy using concentrated solar power and thermochemical

* Corresponding authors. Tel.: +966 13 8603123 (S.A.M. Said). Tel.: +1 519 8884567 (D.S.A. Simakov). Tel.: +1 617 2537090 (Y. Román-Leshkov).
E-mail addresses: samsaid@kfupm.edu.sa (S.A.M. Said), dsimakov@uwaterloo.ca (D.S.A. Simakov), yroman@mit.edu (Y. Román-Leshkov).
[1] These authors contributed equally.

http://dx.doi.org/10.1016/j.solener.2015.11.038
0038-092X/

Nomenclature

$A_{cs,T}$	cross-sectional area of the reformer tube, m^2
A_j	pre-exponential factor of the rate coefficient of reaction j, units of k_j
A_{H_2}	membrane permeability to H_2, mol/(m^2 s $bar^{0.5}$)
A_M	membrane surface area, m^2
A_T	reformer tube surface area, m^2
B_j	pre-exponential factor of the adsorption coefficient of species i, units of K_j
C_p	heat capacity, kJ/(kg K)
d_p	catalytic pellet diameter, m
D_e	effective diffusion coefficient, m^2/s
E_{H_2}	membrane activation energy for H_2 permeation, kJ/mol
E_j	activation energy of reaction j, kJ/mol
f	methane conversion
F_i	molar flow rate of species i, mol/s
$\vec{g}$	gravitational acceleration, m/s^2
G	gravimetric (mass) flow rate, kg/s
GHSV	gas hourly space velocity, h^{-1}
h_i	specific enthalpy of species i, kJ/kg
ΔH_i	adsorption enthalpy change of species i, kJ/mol
J_{H_2}	hydrogen flux through the membrane, mol/(m^2 s)
k_e	effective thermal conductivity, kJ/(m s K)
k_j	rate constant of reaction j, units of Eq. (15)
K_i	adsorption constant of species i, units of Eq. (15)
$K_{j,eq}$	equilibrium constant of reaction j, units of Eq. (15)
L	reformer length, m
m_i	mass fraction of species i
M_i	molecular weight of species i, kg/mol
p	fluid pressure, N/m^2
p_i	partial pressure of gaseous species i, bar
$p_{H_2,M}$	H_2 partial pressure at the permeate side, bar
P	pressure at the outlet of the reaction zone, bar
P_M	pressure at the outlet of the permeate zone, bar
R_j	rate of reaction j, mol/(kg s)
R_g	gas constant, kJ/(mol K)
R_{H_2}	hydrogen recovery
S_i	source term, kg/(m^3 s)
S/C	steam-to-carbon feed ratio
T	temperature, K
u	fluid velocity, m/s
V_T	reformer tube volume, m^3
W_c	catalyst bed weight, kg

Greek letters

α_{ij}	stoichiometric coefficient of species i in reaction j
ε	catalyst bed porosity
μ_f	fluid viscosity, (N s)/m^2
ρ_c	catalyst bed density, kg/m^3
ρ_f	fluid density, kg/m^3
ρ_m	molar density of ideal gas, mol/m^3
$\bar{\bar{\tau}}$	viscous stress tensor, N/m^2

Subscripts

eq	equilibrium
f	feed
M	membrane
MS	molten salt
out	outlet
SG	sweep gas
T	reformer tube

Abbreviations

CFD	computational fluid dynamics
MSR	methane steam reforming
WGS	water gas shift

conversion routes, such as reforming of natural gas (Simakov et al., 2015). Methane (the main component of natural gas) can be converted into synthesis gas (a mixture of carbon monoxide and hydrogen) by steam reforming, as shown below:

$$CH_4 + H_2O \rightleftarrows CO + 3H_2 \quad \Delta H^\circ_{298} = 206\ \text{kJ/mol} \tag{1}$$

$$CO + H_2O \rightleftarrows CO_2 + H_2 \quad \Delta H^\circ_{298} = -41\ \text{kJ/mol} \tag{2}$$

$$CH_4 + 2H_2O \rightleftarrows CO_2 + 4H_2 \quad \Delta H^\circ_{298} = 165\ \text{kJ/mol} \tag{3}$$

The highly endothermic methane steam reforming reaction (MSR, Eq. (1)) is accompanied by the mildly exothermic water gas shift reaction (WGS, Eq. (2)) resulting in an overall endothermic process (Eq. (3)) that requires large heat inputs. In industrial plants, reformer tubes packed with Ni/Al_2O_3 catalyst are heated (typically to temperatures of 850–950 °C) by burning a fraction of natural gas (ca. 30%). An attractive alternative is using concentrated solar energy to provide the required heat to drive the reaction (Simakov et al., 2015; Piatkowski et al., 2011; Romero and Steinfeld, 2012; Agrafiotis et al., 2014; Steinfeld, 2005), thus saving the otherwise combusted fraction of the natural gas (Simakov et al., 2015). The resulting "solar fuel" (with much higher heating value) can be used for electricity generation in gas turbines or as a chemical feedstock.

The choice of solar concentrator for thermochemical natural gas conversion has been historically limited to point-focus concentrators (solar dishes and central receivers) (Piatkowski et al., 2011; Romero and Steinfeld, 2012; Agrafiotis et al., 2014; Steinfeld, 2005) since they can provide the high temperatures (up to 1000 °C) required for MSR. However, these solar collectors have restricted

economic viability due to high capital investment costs. An alternative solution is to use relatively inexpensive and technologically mature solar parabolic troughs, which apply solar heat to the reformer indirectly via a molten salt heat transfer fluid (Giaconia et al., 2008, 2013; Falco et al., 2009; Falco and Piemonte, 2011; Said et al., 2015). Molten salts are advantageous over conventional heat carriers, such as steam and mineral oils, due to higher operating temperatures, low working pressure, high density and heat capacity, and non-flammability. However, linear-focus parabolic trough concentrators can only provide temperatures of ca. 400–600 °C for which the MSR equilibrium predicts CH_4 conversions well below 50% (Simakov et al., 2015).

This equilibrium limitation can be overcome by the use of a membrane reformer in which H_2 is selectively and continuously removed from the reactive stream, shifting the equilibrium toward the formation of products according to Le Chatelier's principle (Uemiya et al., 1991; Chibane and Djellouli, 2011; Fernandes and Soares, 2006; Sheintuch and Simakov, 2011; Simakov and Sheintuch, 2009). Selective removal of H_2 can be effectively done by means of Pd-based membranes (Holleck, 1970; Yun and Oyama, 2011) and complete CH_4 conversions are accessible below 600 °C (Simakov and Sheintuch, 2011), thereby enabling the use of parabolic troughs. Though the cost of Pd is a prohibitive factor, recent developments provide a potential for mass production of Pd-based membranes at economically feasible costs (Sheintuch and Simakov, 2011; Patrascu and Sheintuch, 2015). Importantly, there is no additional energy investment for creating a pressure drop required for H_2 separation (ca. 10 bar), since natural gas is already piped at pressures that exceed this requirement.

The concept of a molten salt-heated membrane reformer integrated into a parabolic trough solar facility (Said et al., 2015) is shown in Fig. 1. Natural gas and steam are fed into the catalytic packed bed tube equipped with the inner H_2-selective membrane tube and surrounded by the shell compartment where the heated molten salt flows co-currently. Steam is fed into the membrane tube to facilitate H_2 separation as a sweep gas, which can be then separated by simple condensation and recycled. Two product streams are generated: upgraded natural gas (a mixture of H_2, CO, CO_2 and unreacted CH_4) and high purity "solar hydrogen". Both streams can be used for power generation using gas turbines or as chemical feedstocks, while H_2 can be also used for highly efficient and ultra-clean electricity generation using fuel cells with water as the only byproduct (Balat, 2008). H_2 is an indispensable feedstock for the chemical industry (Armor, 1999; Crabtree et al., 2004; Ewan and Allen, 2005; Holladay et al., 2009), and, as a fuel, it has many advantages over fossil-based hydrocarbons. However, since no large scale H_2 storage and transportation infrastructure currently exists, it is typically used near the production site.

Membrane reformers for H_2 generation were a subject of experimental and numerical investigations for decades (Sheintuch and Simakov, 2011; Simakov and Sheintuch, 2009, 2011, 2008, 2010; Holleck, 1970; Yun and Oyama, 2011; Coroneo et al., 2010, 2009; Goto et al., 2000; Kyriakides et al., 2013; Falco et al., 2007); a brief overview can be found in our recently published work (Said et al., 2015). However, the feasibility of the integrated concept shown in Fig. 1 is still to be validated. A recent experimental investigation by Patrascu and Sheintuch showed that a Pd membrane reformer packed with the Pt–Ni/CeO_2 (3 wt% Pt, 10 wt% Ni) catalyst supported on a SSiC ceramic foam specifically designed for molten salt heating (to improve heat transfer) provided over 90% CH_4 conversion and over 80% H_2 recovery at 525 °C Patrascu and Sheintuch (2015). Although the heat was provided by an electrical furnace and the use of 3 wt% Pt is questionable from the point of view of economic feasibility, the reformer showed good performance. Generally speaking, platinum group metals have been identified as excellent low-temperature reforming catalysts (Angeli et al., 2014) but their implementation is hindered by the exceedingly high cost associated with current catalyst formulations (typically 1–5 wt%) (Simakov

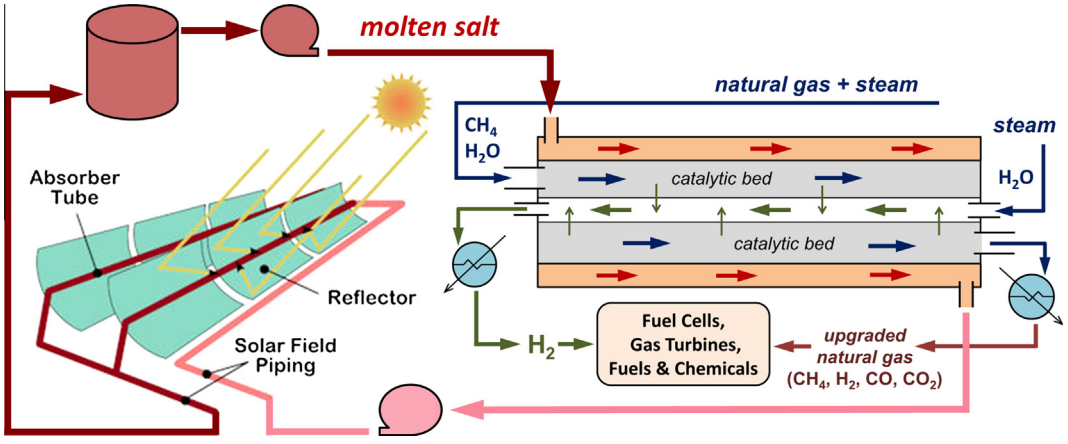

Fig. 1. Simplified schematic sketch of the molten salt-heated membrane reformer integrated with a solar parabolic trough facility.

et al., 2015). Commercial MSR catalysts (10–15 wt% Ni supported on α-Al_2O_3) are inexpensive and features reasonably high catalytic activity, while coking can be effectively prevented by high steam-to-carbon ratios in the feed (ca. 2.5–4) (Joensen and Rostrup-Nielsen, 2002).

A significant amount of work has been done on modeling of Pd membrane reactors, although simplified 1D plug flow formulations that neglect radial gradients are frequently applied (Giaconia et al., 2008; Chibane and Djellouli, 2011; Fernandes and Soares, 2006; Simakov and Sheintuch, 2011, 2008). Several 2D studies have been reported (Kyriakides et al., 2013; Falco et al., 2007; Rodríguez et al., 2012), focusing however on a very specific set or a narrow range of operating conditions. With respect to the concept introduced above (Fig. 1), it is also essential to consider thermal effects. In our previous work (Said et al., 2015), we combined the 2D computational fluid dynamics (CFD) formulation with a parametric study over a wide range of operating conditions and analyzed the molten salt-heated membrane reformer performance limits. Herein, we investigate the thermal effects using a detailed CFD model in its non-isothermal formulation. We specifically focus on the effects of the molten salt and reforming feed flow rates on temperature gradients and hydrogen distribution, evaluating the reformer performance in terms of conversion, hydrogen recovery and selectivity to carbon monoxide.

2. Membrane reforming equilibrium

We first evaluate the thermodynamic limits by deriving the MSR equilibrium using the approach followed by Simakov et al. (2015). Briefly, extents of species (CH_4, H_2O, CO, CO_2 and H_2) in equilibrium are expressed in terms of CH_4 conversion (f_1), CO yield (f_2), and steam-to-carbon feed ratio (α); these expressions (ϕ_i) are listed in the abovementioned reference Simakov et al. (2015). For the membrane reformer, H_2 partial pressure in the membrane interior ($p_{H_2,M}$) is expressed assuming that the membrane is permselective to H_2 and that the H_2 partial pressure at the membrane side is equal to that at the reforming side, i.e. exit conditions of an infinitely long reactor see Appendix in Simakov and Sheintuch (2011, 2008). Next, equilibrium partial pressures are expressed in terms of extents of species and these expressions are substituted into the definitions of the MSR and WGS equilibrium constants. Details can be found in Simakov et al., see Eqs. (7)–(14) Simakov et al. (2015); membrane reactor equilibrium derivation follows exactly the same approach, except for the expression for H_2 extent at equilibrium which depends on $p_{H_2,M}$ Simakov and Sheintuch (2011, 2008).

The resulting equations for the non-membrane (Eqs. (4) and (5)) and membrane (Eqs. (6) and (7)) reforming systems are provided below. Note that for the membrane reformer, the equilibrium pressure P is defined as the pressure on the reforming side.

$$A_{eq,MSR}\exp\left(\frac{-E_{eq,MSR}}{R_gT}\right)\frac{1}{P^2} = \frac{f_2(4f_1-f_2)^3}{(1-f_1)(\alpha-2f_1+f_2)(1+\alpha+2f_1)^2} \quad (4)$$

$$A_{eq,WGS}\exp\left(\frac{-E_{eq,WGS}}{R_gT}\right) = \frac{(f_1-f_2)(4f_1-f_2)}{f_2(\alpha-2f_1+f_2)} \quad (5)$$

$$\frac{(P-p_{H_2,M})}{p_{H_2,M}^3}A_{eq,MSR}\exp\left(\frac{-E_{eq,MSR}}{R_gT}\right) = \frac{f_2(1+\alpha-2f_1+f_2)}{(1-f_1)(\alpha-2f_1+f_2)} \quad (6)$$

$$\frac{(P-p_{H_2,M})}{p_{H_2,M}}A_{eq,WGS}\exp\left(\frac{-E_{eq,WGS}}{R_gT}\right) = \frac{(f_1-f_2)(3-2f_1+f_2)}{f_2(\alpha-2f_1+f_2)} \quad (7)$$

To calculate the non-membrane equilibrium, Eqs. (4) and (5) are solved numerically for f_1 and f_2 as a function of temperature (T) and pressure (P). Eqs. (6) and (7) are solved to evaluate the membrane reformer equilibrium; parameters A_{eq} and E_{eq} can be found in the literature (Hou and Hughes, 2001). The results are shown in Fig. 2, in terms of CH_4 conversion ($f_1 = (n_{CH_4,f} - n_{CH_4,eq})/n_{CH_4,f}$) and selectivity to CO ($S_{CO} \equiv f_2/f_1 = n_{CO,eq}/(n_{CO_2,eq} + n_{CO,eq})$), plotted in the 2D domain of temperature and pressure.

The effect of the membrane separation is remarkable. The non-membrane equilibrium predicts very low CH_4 conversions almost in the entire domain except for very low (industrially irrelevant) pressures for which a reasonably high conversion is achievable only at a relatively high temperature. Introducing a H_2 selective membrane into the system changes the values dramatically, generating near complete conversions even in the low-temperature regime. Importantly, elevated pressures are advantageous for the membrane reformer system since higher pressure drop across the membrane enhances H_2 separation. Separation of H_2 also enhances the WGS reaction (Eq. (2)) resulting in a very low selectivity to CO (Fig. 2b). Note that for the case of $p_{H2,M} = 0.3$ bar, which can be achieved by diluting H_2 in the membrane interior using a sweep gas (Fig. 1), nearly complete conversions can be obtained at temperatures below 800 K. It should be noticed that the results presented in Fig. 2 are equilibrium calculations that do not account for kinetic and transport limitations. Regardless, the difference between the non-membrane and membrane systems is notable.

3. Model formulation

Fig. 3 shows the two-dimensional CFD computation domain representing the tubular axisymmetric geometry of the molten salt-heated membrane reformer (Fig. 1). The dimensions of the Pd membrane used in a recent experimental work (Patrascu and Sheintuch, 2015), alongside with the corresponding reformer dimensions are listed in Table 1. A

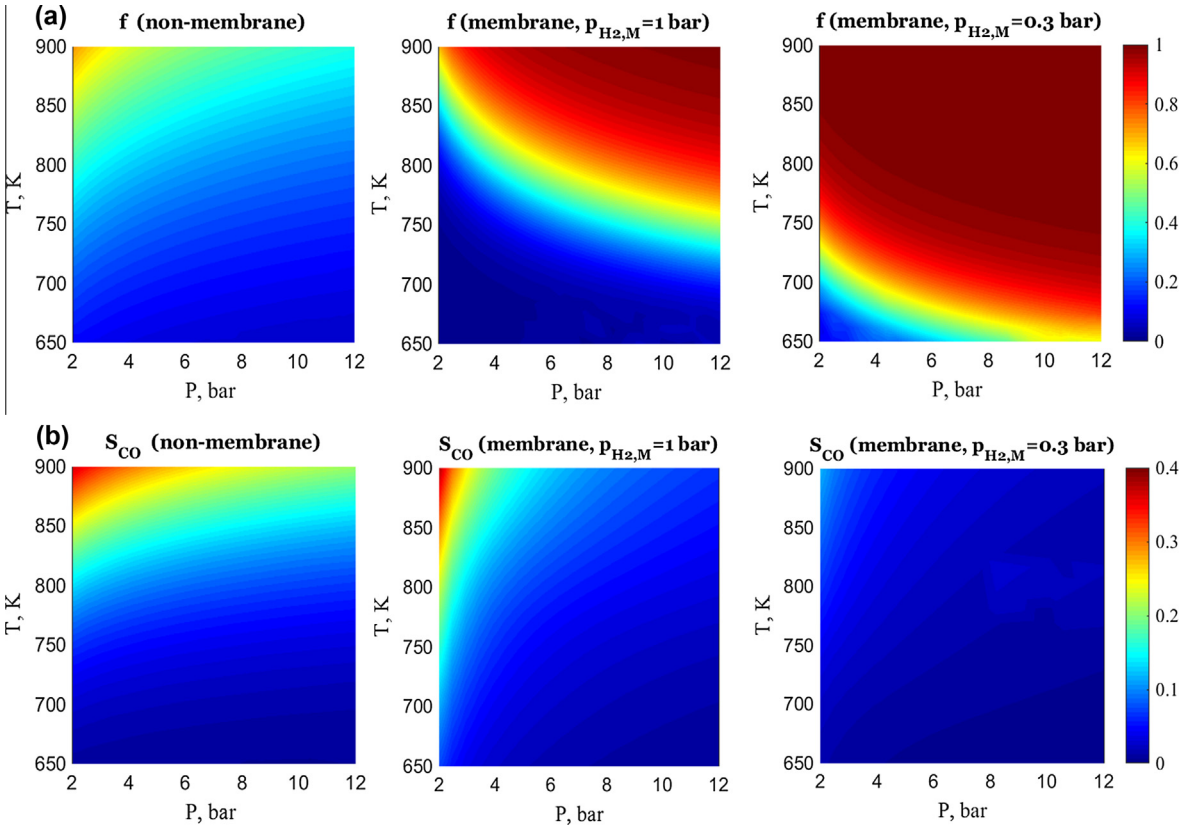

Fig. 2. (a) Equilibrium CH_4 conversions (f) and (b) selectivity to CO (S_{CO}) as a function of T and P for the non-membrane system (left panels) and the membrane reformer with a membrane interior H_2 partial pressure of 1 bar (middle panels) and 0.3 bar (right panels).

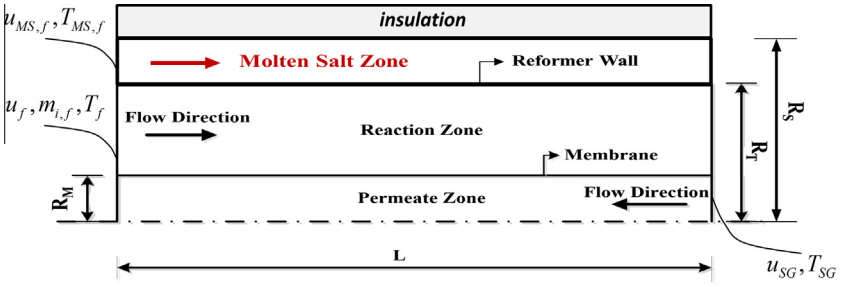

Fig. 3. CFD computational domain (not to scale): a two-dimensional cut representing the tubular axisymmetric geometry of the molten salt-heated membrane reformer (Fig. 1); R_M, R_T, R_S stand for the membrane, reformer tube, and molten salt shell radii, respectively, and L is the reformer length. Boundary conditions are defined as feed fluid velocity, composition, and temperature, applying continuity across the reformer wall (for heat transfer) and insulation along the molten salt shell wall.

Table 1
Reformer dimensions.

D_M (cm)	D_T (cm)	D_S (cm)	L (cm)	A_M (cm^2)	V_T (cm^3)	d_p (cm)
1.4	5	7	40	176	785	0.3

D and L denote diameter and length of the tubular membrane, packed bed and molten salt compartments (Figs 1 and 3). A_M and V_T denote the membrane area and the reformer tube volume, d_p stands for the (spherical) catalytic pellet size; subscripts M, T and S stand for membrane, reformer tube, and molten salt shell, respectively.

mixture of CH_4 and H_2O is fed to the reaction zone, where it is converted into H_2, CO and CO_2 over the catalytic packed bed. The H_2 permeated through the Pd membrane is actively removed by steam, which is fed in counter-current mode (Fig. 1) to keep high H_2 partial pressure difference across the membrane.

Detailed formulation of the steady-state 2D CFD model implemented in this study can be found in our previous work

(Said et al., 2015). We assume a pseudo-homogeneous description of the axisymmetric catalytic bed, i.e. the computational domain representing the catalytic packed bed is solved as a continuum. Catalyst and membrane deactivation are not accounted for in the present study that focuses on thermal management and reformer throughput optimization. The model comprises the equations for continuity (Eq. (8)), momentum balance (Eq. (9)), energy balance (Eq. (10)) and mass balance for gaseous species i (Eq. (11)):

$$\nabla \cdot (\varepsilon \rho_f \vec{u}) = S_i \tag{8}$$

$$\nabla \cdot (\rho_f \vec{u}\vec{u}) = -\nabla p - \beta \vec{u} + \nabla \cdot \vec{\vec{\tau}} + \rho_f \vec{g} \tag{9}$$

$$\nabla \cdot (\rho_f \vec{u} h + \vec{u} p) = \nabla \cdot \left(k_e \nabla T - \sum_i h_i j_i + \vec{\vec{\tau}} \cdot \vec{u}\right) + (1-\varepsilon)\rho_c \sum_j R_j \Delta H_j \tag{10}$$

$$\nabla \cdot (\varepsilon \rho_f \vec{u} m_i) = \nabla (\rho_f D_e \nabla m_i) + (1-\varepsilon)\rho_c M_i \sum_j \alpha_{ij} R_j + S_i \tag{11}$$

In the equations above, m_i stands for the mass fraction of species i, R_j is the reaction rate with a stoichiometric coefficient α_{ij}, ε is the packed bed void fraction, k_e and D_e are effective conductivity and diffusivity (Simakov and Sheintuch, 2011, 2008) and S_i is the source/sink term. There is no catalyst in the molten salt compartment and in the permeate zone ($\varepsilon = 1$) and, therefore, there is no reaction there ($R_j = 0$). There is no gas flow in the molten salt zone, therefore $m_i = 0$ and $S_i = 0$ in this compartment.

The packed bed friction coefficient is given by the following equation ($\varepsilon = 0.5$, $d_p = 0.003$ m):

$$\beta = \frac{150\mu_f (1-\varepsilon)^2}{\varepsilon^3 d_p^2} + \frac{1.75(1-\varepsilon)\rho_f}{\varepsilon^3 d_p} |\vec{u}|\ |\vec{u}| = \sqrt{u_r^2 + u_z^2} \tag{12}$$

Reaction rates are calculated using the commonly adopted kinetics for MSR over the Ni/Al_2O_3 catalyst (Xu and Froment, 1989a, 1989b), Eqs (13a)–(13f). All parameters are tabulated in the literature, e.g. see Tables 3 and 4 in Rodríguez et al. (2012). Intraparticle and interphase transport limitations can be neglected for the size of catalytic pellets used in our simulations ($d_p = 0.3$ cm, Table 1) (Simakov and Sheintuch, 2011).

$$R_1 = \frac{k_1}{p_{H_2}^{2.5}} \left(p_{CH_4} p_{H_2O} - \frac{p_{H_2}^3 p_{CO}}{K_{1,eq}}\right) \frac{1}{den^2} \tag{13a}$$

$$R_2 = \frac{k_2}{p_{H_2}} \left(p_{CO} p_{H_2O} - \frac{p_{H_2} p_{CO_2}}{K_{2,eq}}\right) \frac{1}{den^2} \tag{13b}$$

$$R_3 = \frac{k_3}{p_{H_2}^{3.5}} \left(p_{CH_4} p_{H_2O}^2 - \frac{p_{H_2} p_{CO_2}}{K_{3,eq}}\right) \frac{1}{den^2} \tag{13c}$$

$$den = 1 + K_{CO} p_{CO} + K_{H_2} p_{H_2} + K_{CH_4} p_{CH_4} + \frac{K_{H_2O} p_{H_2O}}{p_{H_2}} \tag{13d}$$

$$k_j = A_j \exp\left(\frac{-E_j}{R_g T}\right) \tag{13e}$$

$$K_i = B_i \exp\left(\frac{-\Delta H_i}{R_g T}\right) \tag{13f}$$

The source (sink) term that accounts for membrane separation is given by the following equation ($S_i = 0$ for $i \neq H_2$ for H_2 selective membrane):

$$S_i = \frac{A_M J_{H_2} M_{H_2}}{V_T} \tag{14a}$$

$$J_{H_2} = A_{H_2} \exp\left(-\frac{E_{H_2}}{R_g T}\right) \left(p_{H_2}^{0.5} - p_{H_2,M}^{0.5}\right) \tag{14b}$$

The H_2 permeation activation energy ($E_{H_2} = 11$ kJ/mol) and membrane permeability ($A_{H_2} = 5.6$ mol/(m^2 s bar$^{0.5}$)) were adopted from the recent experimental work by Patrascu and Sheintuch (2015).

Steady-state numerical simulations were performed applying standard boundary conditions (Fig. 3) using the commercial CFD package Fluent 14.0 (ANSYS Inc., PA, USA) (FLUENT). The source term S_i was set to zero unless the computational cell is adjacent to the membrane, i.e., to the boundary between the reaction zone and the permeate zone (Fig. 3). The pressure-velocity correction was done using the SIMPLE algorithm. Reaction rates and H_2 permeation were modeled by user-defined functions (C++) compiled and hooked in the Fluent software. Dependences of fluid density, viscosity, heat capacity, specific enthalpy, diffusivity, and thermal conductivity on temperature, pressure and composition were accounted for by built-in functions of the computation software using standard definitions (Younglove, 1982; Younglove and Ely, 1987). Thermophysical properties of the solar molten salt ($NaNO_3/KNO_3$, 60/40 wt%) was adopted from the literature (Kearney et al., 2003).

4. Results and discussion

In all simulations, outlet pressures of the reforming and membrane zone were set to 10 and 1 bar, respectively, and the feed steam-to-carbon ratio was set to 3 to prevent coking (Simakov et al., 2015). The sweep gas was assumed to be steam, with its mass flow rate being equivalent to that of the total reforming feed, to lower the H_2 partial pressure in the membrane interior, thus facilitating H_2 separation and enhancing CH_4 conversion (Fig. 2). In a practical situation, H_2 can be separated from the membrane outlet stream simply by condensation with water being recycled. All operating conditions are listed in Table 2. Maximum temperature was selected according to the upper temperature limit provided by molten salts; previous experimental works have demonstrated that Pd-based membranes can be safely operated at temperatures even exceeding this limit and at 10 bar (Simakov and Sheintuch, 2009, 2010; Patrascu and Sheintuch, 2015).

Reformer performance was evaluated as a function of the feed space velocity (GHSV, Eq. (15)) and the heat supply rate, i.e. molten salt feed temperature ($T_{MS,f}$) and gravimetric flow rate (G_{MS}); ranges are shown in Table 2. To estimate the reference molten salt mass flow rate ($G_{MS,0}$), we require that the rate of the molten salt sensible

Table 2
Operating conditions.

P_T (bar)	P_M (bar)	S/C	$G_{SG}/G_{T,f}$	T_{SG} (K)	$T_{MS,f}$ (K)	$G_{MS}/G_{MS,0}$	GHSV (h^{-1})
10	1	3	1	375	673–873	1–10	1000–80,000

P_T and P_M denote outlet pressures of the reforming and membrane compartments; S/C is the feed steam-to-carbon ratio. G_{SG} and T_{SG} stand for the sweep gas mass flow rate and inlet temperature; $G_{T,f}$ stands for the reformer tube total feed mass flow rate. Variable parameters are molten salt inlet temperature ($T_{MS,f}$), gravimetric flow rate (G_{MS}), and feed space velocity (GHSV). $G_{MS,0}$ is the reference molten salt supply rate defined by Eq. (16).

heat supply ($\rho_{MS} = 1899$ kg/m^3, $C_{p,MS} = 1.495$ kJ/(kg K) Kearney et al., 2003) is similar to the rate of heat consumption by MSR (Eq. (16), ρ_m is the molar density of ideal gas) (Said et al., 2015). This reference molten salt supply rate is calculated assuming 50% conversion and that the molten salt temperature drops to a half of its feed value at the reactor exit (Eq. (16)).

$$\mathrm{GHSV} = \frac{u_f A_{cs,T}}{V_T} \tag{15}$$

$$G_{MS,0} \equiv u_{MS,0}\rho_{MS}A_T = \frac{0.5F_{MSR,f}(\Delta H_{MSR} + \Delta H_{WGS})}{0.5C_{p,MS}T_{MS,f}}$$

$$F_{MSR,f} = u_f A_{cs,T}\rho_m \tag{16}$$

Methane conversion, selectivity to CO, and pure H_2 yield (H_2 recovery by the membrane) are defined by Eqs (17)–(19), respectively, in terms of feed and outlet molar flow rates:

$$f_{CH_4} = \frac{F_{CO,out} + F_{CO_2,out}}{F_{CH_4,f}} \tag{17}$$

$$S_{CO} = \frac{F_{CO,out}}{F_{CO,out} + F_{CO_2,out}} \tag{18}$$

$$Y_{H_2} = \frac{F_{H_2,M,out}}{F_{CH_4,f}} \tag{19}$$

4.1. Approach to equilibrium: membrane vs. non-membrane

We first investigate the case of excess heat supply ($G_{MS}/G_{MS,0} = 10$) and low space velocity (GHSV = 1000 h^{-1}), when conversions close to equilibrium are expected. Fig. 4 shows representative temperature and H_2 mass fraction profiles within the non-membrane reformer. As expected, temperature drops significantly at the reactor inlet as the highly endothermic reforming process takes place. However, since heat is supplied in excess (as it is evident from only a minor temperature drop in the molten salt compartment) both the reformer and molten salt compartment outlets are at the temperature of the molten salt feed. Hydrogen concentration is slightly lower at the reformer inlet and along the reformer wall, reflecting reaction kinetics and transport processes (convection and dispersion), but nearly uniform due to the low space velocity (long residence time) used.

Temperature and H_2 concentration profiles look very different in the membrane reformer simulation shown in Fig. 5, which was performed under identical conditions except for the presence of the membrane. Interestingly, nearly uniform distributions are obtained in the reformer compartment for both temperature and H_2 mass fraction due to the effect of H_2 separation carried out in a counter-current mode. The lower temperature at the membrane inlet is due to the cooling effect of the sweep gas (steam) that is fed at relatively low temperature (Table 2).

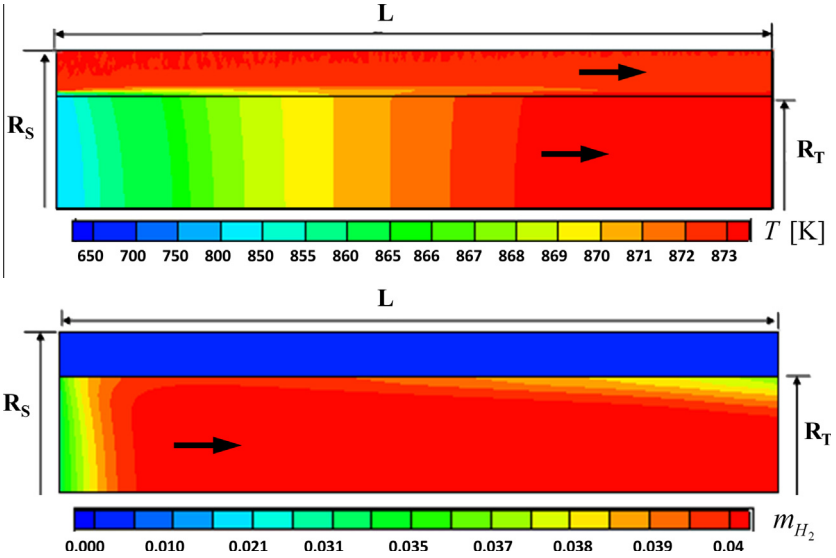

Fig. 4. Approach to equilibrium (low space velocity and excess heat supply) for the non-membrane reformer: temperature gradients (upper panel) and H_2 mass fraction (lower panel) obtained with $T_{MS,f} = 873$ K, GHSV = 1000 h^{-1} and $G_{MS}/G_{MS,0} = 10$.

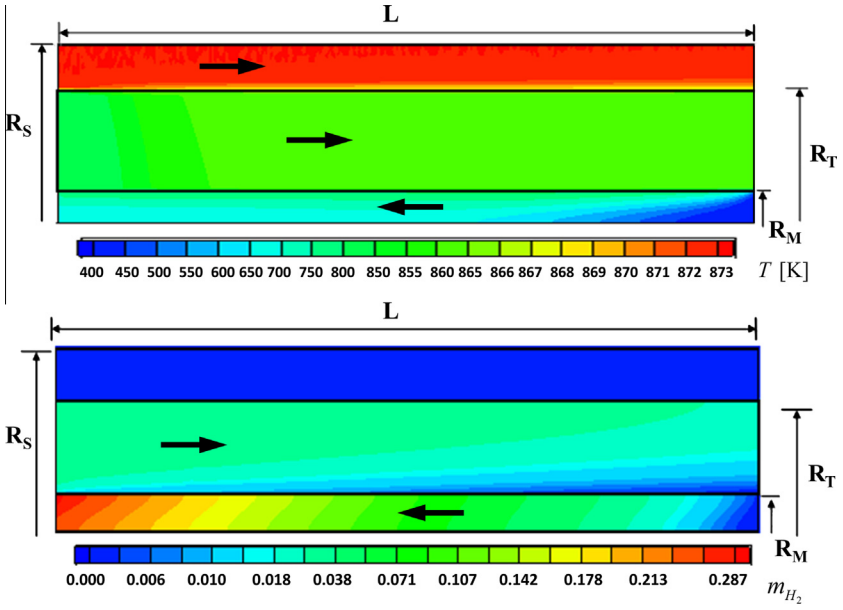

Fig. 5. Approach to equilibrium (low space velocity and excess heat supply) for the membrane reformer: temperature gradients (upper panel) and H_2 mass fraction (lower panel) obtained at $T_{MS,f} = 873$ K, GHSV = 1,000 h^{-1} and $G_{MS}/G_{MS,0} = 10$.

Table 3
Approach to equilibrium.

	Numerical simulations results				Equilibrium values			
	Non-membrane		Membrane		Non-membrane		Membrane	
$T_{MS,f}$	773 K	873 K	773 K	873 K	773 K	873 K	773 K	873 K
f_{CH_4}	0.18	0.35	0.75	0.99	0.19	0.36	0.64	0.97
S_{CO}	0.053	0.203	0.025	0.104	0.048	0.170	0.030	0.068
Y_{H_2}	–	–	2.81	3.44	–	–	2.54	3.81

Simulated results listed in the table were extracted from numerical simulations performed at low space velocity (GHSV = 1000 h^{-1}) and excess heat supply ($G_{MS}/G_{MS,0} = 10$). Equilibrium values are shown for comparison (for reformer outlet pressure of 10 bar and assuming a membrane interior H_2 partial pressure of 1 bar).

As expected, H_2 content is low in the membrane interior at the membrane inlet and H_2 is accumulated along the axial dimension as it is separated from the reaction mixture.

Results of simulations performed for two different molten salt inlet temperatures are shown in Table 3 for the non-membrane and membrane modes of operation, alongside with equilibrium values calculated using Eqs. (4)–(7). First, the numerical simulations predict a drastic improvement in CH_4 conversion and a substantial decrease in CO selectivity for the membrane reformer compared to the non-membrane reformer, in accordance with the equilibrium predictions shown in Fig. 2. Moreover, the results of the numerical simulations are in good quantitative agreement with equilibrium values for the non-membrane reformer (Table 3) for which the reforming stream exits the reactor at the temperature of the molten salt feed. For the membrane reformer, the difference between the simulated values and the equilibrium values is higher (Table 3), but still in good agreement, considering that a membrane interior H_2 partial pressure of 1 bar is used in the equilibrium calculations and a slightly lower outlet temperature was obtained in the simulated membrane reformer (Fig. 5). Taken together, these data show that the model is well-defined and is able to predict equilibrium values under conditions of excess heat supply and long residence times.

4.2. Molten salt-heated membrane reformer: typical profiles

For process optimization, it is highly desirable to minimize the molten salt flow rate (to reduce energy investment in pumping and storage) and, at the same time, to maximize the steam reforming feed rate (to increase reformer throughput), while keeping high CH_4 conversion and H_2 recovery. These two objectives are rather contradicting: reducing the molten salt supply rate will eventually lead to decreasing reformer temperatures and, thus, lower conversions and H_2 recovery. Figs 6 and 7 show typical profiles obtained for the membrane reformer at GHSV = 30,000 h^{-1} and $G_{MS}/G_{MS,0} = 1$. As expected for the packed bed reactor configuration, the velocity profile in the reaction zone is nearly uniform. The velocity field in the molten salt compartment is also uniform. In the membrane interior, an expected increase in the velocity is observed due to the separated H_2 accumulation along the axial dimension (Fig. 6). As a

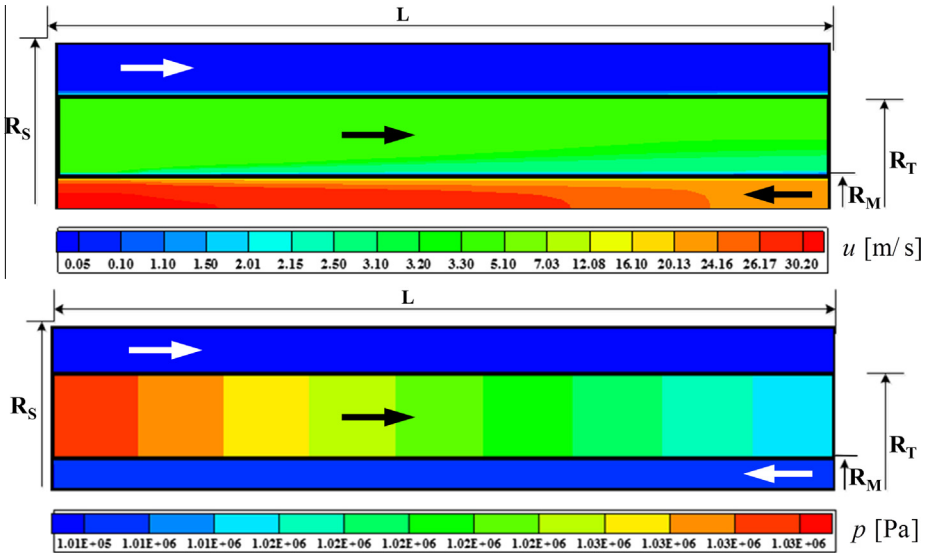

Fig. 6. Velocity profile (upper panel) and pressure field (lower panel) in the membrane reformer for high space velocity and limited heat supply; $T = 873$ K, GHSV $= 30{,}000\ h^{-1}$ and $G_{MS}/G_{MS,0} = 1$.

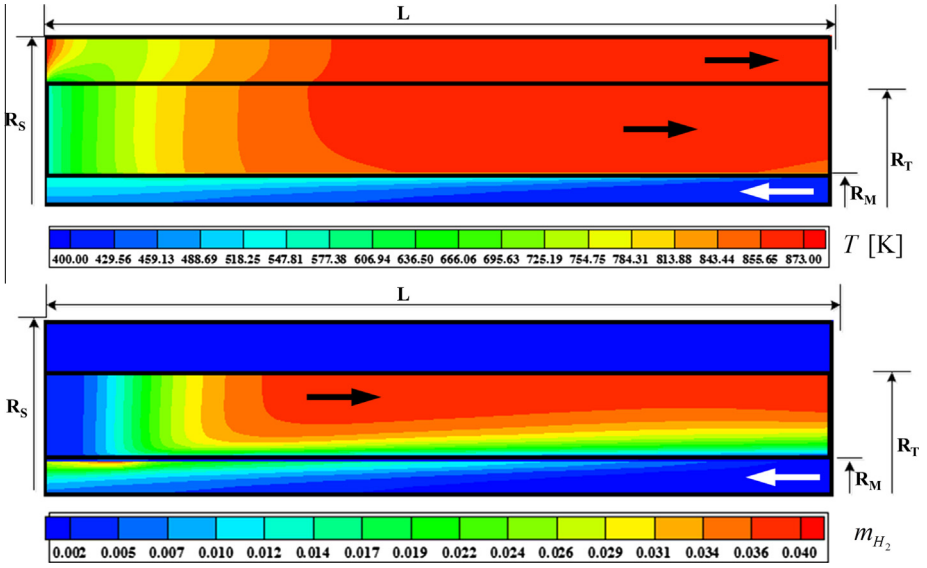

Fig. 7. Temperature (upper panel) and hydrogen fraction (lower panel) distributions in the membrane reformer for high space velocity and limited heat supply; $T = 873$ K, GHSV $= 30{,}000\ h^{-1}$ and $G_{MS}/G_{MS,0} = 1$.

consequence of H_2 separation, the reaction zone pressure decreases substantially (Fig. 6) despite the total increase in the number of moles in the reforming process (Eq. (3)).

For these conditions, temperature and concentration profiles are quite complex (Fig. 7). As a result of high feed flow rate and low rate of molten salt supply, there is a significant temperature drop at the reformer entrance in both the reaction and molten salt compartments, wherein nearly half of the reformer is cooled down significantly, to ca. 600–750 K. Further downstream, there is essentially no reaction, as it is evident from the temperature rise along the axial dimension followed by the equilibration between the reaction and molten salt compartments. The appearance of such significant axial temperature gradients may have a negative effect on membrane durability due to the varying thermal expansion of the membrane material along the axial direction and may eventually lead to mechanical damage to the membrane.

The membrane interior is at much lower temperature due to the high flow rate of steam that is fed to the membrane at low temperature. Note that in all simulations sweep gas flow rate is increased to match the increased feed flow rate in the reformer compartment, Table 2. Hydrogen concentration is very low at the reformer entrance because H_2 separation is carried out counter-currently with a high sweep gas flow rate (Fig. 7). However, the overall H_2

recovery is not efficient since the reformer compartment outlet still contains a large fraction of (unseparated) H_2, as it is evidently reflected in the overall reformer performance (as discussed in Section 4.3).

4.3. Effects of temperature and space velocity on reformer performance

Fig. 8 shows the effect of the molten salt inlet temperature (keeping $G_{MS}/G_{MS,0} = 1$) in terms of the overall reformer performance, i.e. CH_4 conversion, selectivity to CO and H_2 recovery (Eqs (17)–(19)), upon reducing space velocity to GHSV = 5000 h^{-1}. A general trend of increasing conversion, selectivity, and H_2 recovery is observed as a function of temperature. Specifically, at the upper limit of temperatures obtainable by solar parabolic troughs (873 K), nearly complete CH_4 conversion and very high H_2 recovery of 3.3 are achieved. The stoichiometric maximum H_2 recovery is 4 for complete CH_4 conversion and no CO formation, Eq. (3). Decreasing the temperature below 773 K is not favorable, although reasonably high conversions of 0.5–0.7 and H_2 recovery of 1.8–2.6 are obtained. Note that a 50% CH_4 conversion will still result in a substantial degree of fuel upgrading (Simakov et al., 2015), while also providing a stream of high purity H_2 (2 moles per mole of CH_4 fed). These results not only demonstrate the potential of the solar membrane reforming process (preliminary techno-economic evaluation will be discussed in Section 4.5), but also emphasize the importance of the molten salt storage facility (Fig. 1) for regulating temperature fluctuations that result from the transient nature of solar irradiation.

For the membrane reformer configuration analyzed in our study, increasing the space velocity beyond GHSV = 5000 h^{-1} is rather unfavorable, as can be concluded from analyzing the data shown in Fig. 9. A sharp drop in the reformer performance occurs in the GHSV range between 1000 and 5000 h^{-1}, where the conversion decreases almost two-fold, followed by a further moderate decrease. H_2 recovery follows a similar trend. The fact that the conversion almost attains its non-membrane equilibrium values after the initial drop (see Fig. 2 for equilibrium values) suggests that the reformer performance is limited by the membrane separation ability (Said et al., 2015).

4.4. Optimization

Temperature and concentration profiles obtained for the reformer operated in the intermediate regime (GHSV = 5000 h^{-1} and 10,000 h^{-1}) with a moderately increased heat supply ($G_{MS}/G_{MS,0} = 3$) are shown in Figs 10 and 11. For the case of GHSV = 10,000 h^{-1} (Fig. 10), the temperature distribution is qualitatively similar to that shown in Fig. 7, despite the three-fold decrease in the feed flow rate and the increase in molten salt supply rate. As expected, under these conditions the section of the reactor that undergoes a significant temperature drop was reduced (compare upper panels of Figs 7 and 10). Consequently, the reformer performance was improved given that a larger fraction of the reaction compartment is at a high temperature, as evidenced from the improved H_2 separation (compare bottom panels of Figs 7 and 10) and the lower fraction of H_2 in the reaction compartment outlet in Fig. 10.

Reducing space velocity to GHSV = 5000 h^{-1} leads to very different temperature and concentration distribution (Fig. 11). The reaction zone is now nearly isothermal, except for the small zone adjacent to the reformer inlet and a significant part of the membrane interior is at high temperature. Such thermal profile is favorable for both reforming reaction and H_2 separation. The reaction compartment has nearly uniform and relatively low H_2 content, while the H_2 fraction in the membrane interior is significantly higher with H_2 separation taking place along almost the entire membrane length (Fig. 11).

Table 4 summarizes the reformer performance for the two cases discussed above in terms of conversion, selectivity and H_2 recovery, showing also the reformer output in terms of power density and fuel upgrade. To calculate the power density, it is assumed that the separated H_2 is used to drive a fuel cell stack (Simakov and Sheintuch, 2011):

$$P = \frac{\eta_{FC}\Delta G_{FC} F_{H_2,M,out}}{V_r} \tag{20}$$

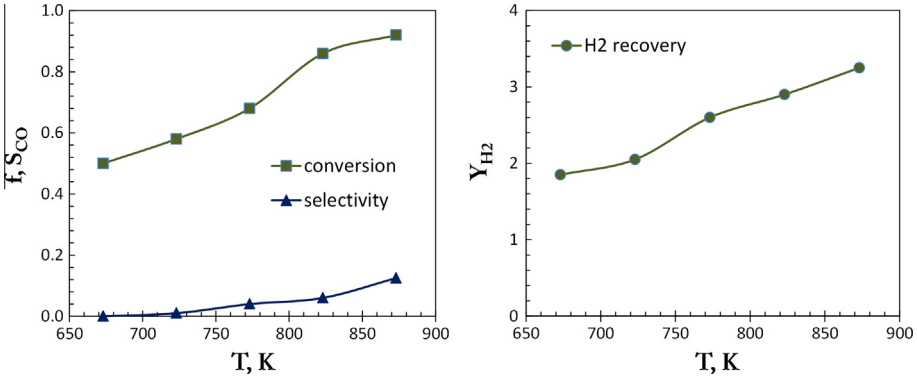

Fig. 8. Effect of the molten salt feed temperature on conversion, selectivity to CO and H_2 recovery; GHSV = 5000 h^{-1} and $G_{MS}/G_{MS,0} = 1$.

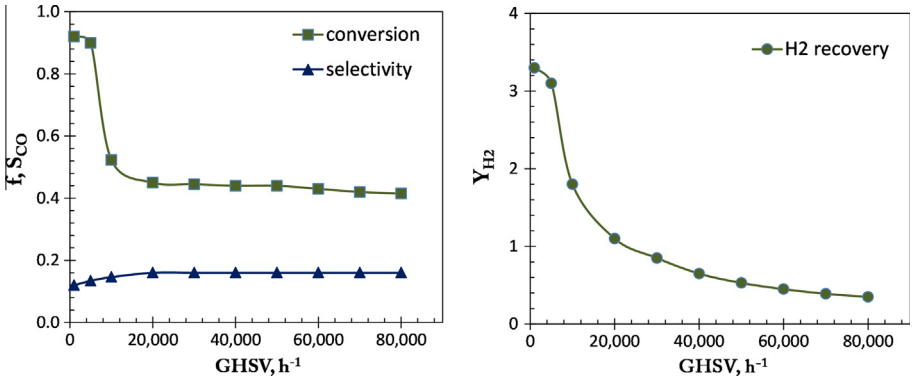

Fig. 9. Effect of space velocity on CH_4 conversion, selectivity to CO and H_2 recovery; $T = 873$ K and $G_{MS}/G_{MS,0} = 1$.

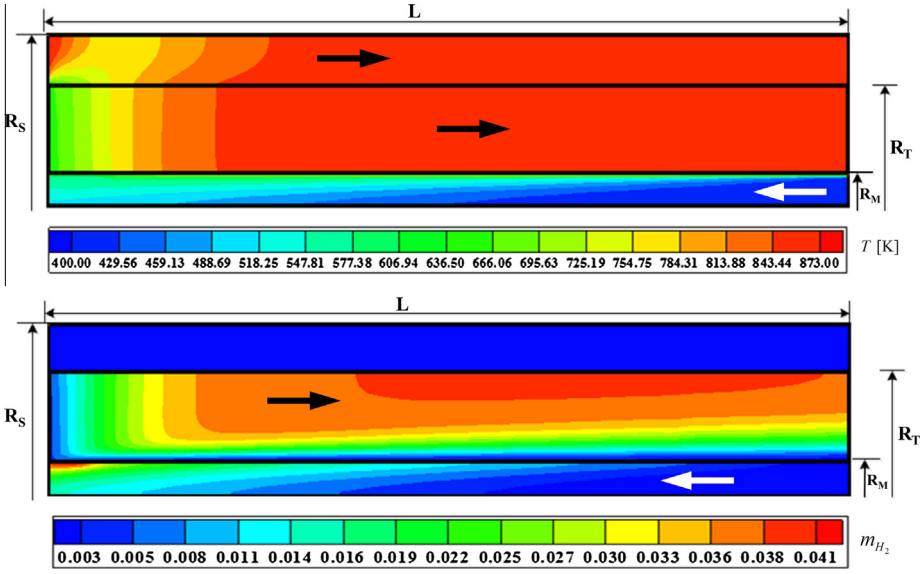

Fig. 10. Temperature (upper panel) and hydrogen fraction (lower panel) distributions in the membrane reformer for $T = 873$ K, GHSV = 10,000 h^{-1} and $G_{MS}/G_{MS,0} = 3$.

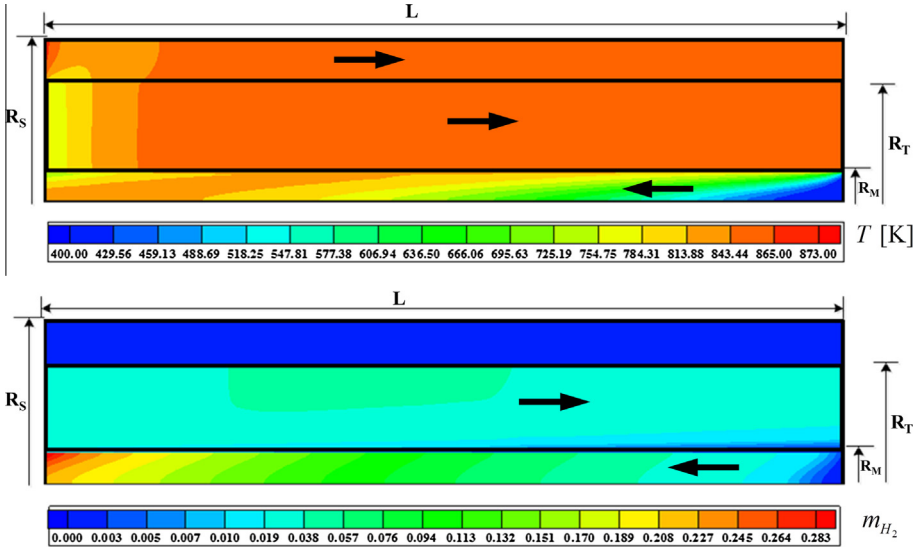

Fig. 11. Temperature (upper panel) and hydrogen fraction (lower panel) distributions in the membrane reformer for $T = 873$ K, GHSV = 5,000 h^{-1} and $G_{MS}/G_{MS,0} = 3$.

Table 4
Reformer performance with optimized operating conditions.

GHSV (h^{-1})	f_{CH4}	S_{CO}	Y_{H2}	P (kW/L)	FU (%)
5000	0.99	0.13	3.49	1.90	39.9
10,000	0.52	0.15	1.44	1.57	21.2

The results listed in the table were extracted from simulations performed at $T = 873$ K, $G_{MS}/G_{MS,0} = 3$.

In the equation above, $\eta_{FC} = 0.6$ is the fuel cell efficiency and ΔG_{FC} is the Gibbs free energy of the H_2 oxidation reaction. We consider the total reformer volume, i.e. the sum of the membrane, reaction and molten salt compartments (Table 1), assuming also an additional (1.5 cm thick) layer of insulation ($V_r = 3.1$ L). The fuel upgrade (Simakov et al., 2015) is calculated accounting for the total reformer outlet, i.e. reaction compartment outlet combined with separated H_2 (LHV is low heating value, f_1 and f_2 were defined in Section 2):

$$FU = 100\left[\frac{(1-f_1)LHV_{CH_4} + f_2 \cdot LHV_{CO} + (4f_1 - f_2)LHV_{H_2}}{LHV_{CH_4}} - 1\right] \quad (21)$$

The predicted reformer performance is quite outstanding in terms of fuel upgrade and power density, Table 4. Note that GHSV = 5000 h^{-1} corresponds to CH_4 feed of 16.4 NL/min (see Eq. (15); CH_4 feed fraction is 0.25 because S/C = 3, Table 2). For the H_2 recovery shown in Table 4, the outlet pure H_2 output from this 3 L volume unit is predicted to be 57.1 NL/min, which corresponds to a power density of 1.9 kW/L (Table 4). Notably, a high power density is still obtained for a GHSV = 10,000 h^{-1}, despite almost twofold decrease in conversion. This decrease in conversion is compensated by the twofold increase in the reformer throughput, with more H_2 being separated. However, a significant drop in fuel upgrade is observed when compared to the case of GHSV = 5000 h^{-1} (Table 4). Altogether, these predictions demonstrate the promising potential of the solar membrane concept proposed herein. Still, a number of important aspects remain to be investigated for a practical application assessment, such as membrane deactivation and durability, and the price of the H_2 separation membrane. Eventually, the entire system integrating a concentrated solar power facility with membrane reformers should be optimized, considering the total investment cost and evaluating the cost of "solar fuel" production under different circumstances. Such assessment is out of the scope of the present paper, but will be the subject of future work.

4.5. Techno-economic evaluation

We first evaluate the amount of Pd in the membrane used in our study. A simple calculation shows that the Pd content in this 40 cm length and 1.4 cm diameter membrane with the 5 μm thick active Pd layer (Patrascu and Sheintuch, 2015) is 1.05 g which translates to ca. $30 USD considering current prices of Pd and assuming that metal content dominates over manufacturing cost. The price of Ni catalyst is not a concern, but one should remember that high steam-to-carbon ratio is required to prevent coking while using Ni-based catalysts. Another important consideration is compactness, i.e. the amount of fuel upgraded, energy generated, etc. per reactor volume. Fuel upgrade, power density, Pd-based cost, and pure H_2 production rate corresponding to the simulation results shown in Fig. 9 (with $G_{MS}/G_{MS,0} = 1$) are plotted versus reformer throughput in Fig. 12.

Exceptionally high fuel upgrade for GHSV < 10,000 h^{-1} corresponds to the operating regime when the reformer performance is not limited by the membrane separation ability, shifting the equilibrium to a large extent toward the theoretical limit of fuel upgrading (Simakov et al., 2015). With respect to the solar-heated reformer concept shown in Fig. 1, 20–35% percent of the resulting "solar fuel" heating value would be solar energy converted into chemical bonds. In addition, excellent power density is achieved, highlighting the compactness of the system. Even higher power densities are achieved as the reformer throughput is increased (up to 3 kW/L), though the fuel upgrade drops significantly (Fig. 12, left panel). Keeping in mind that power density is calculated solely based on the separated H_2 outlet flow rate

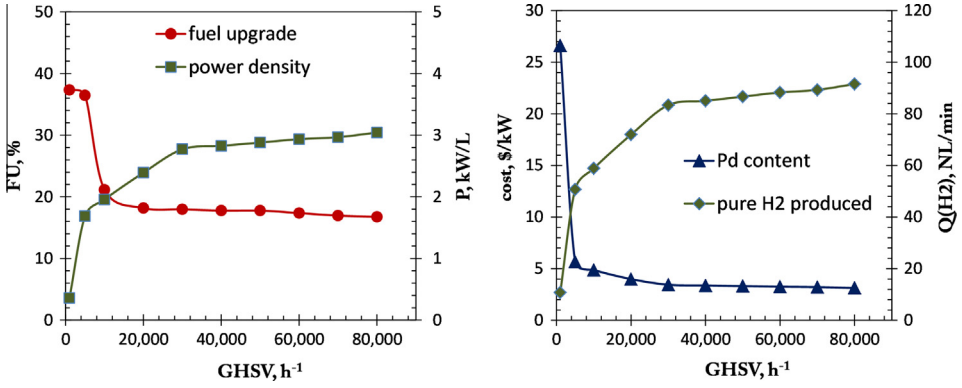

Fig. 12. Reformer performance as calculated from the simulation results presented in Fig. 9. Left panel: fuel upgrade and power density calculated using Eqs (20) and (21). Right panel: cost of Pd (in membrane) per kW power generated (if H_2 fed to a fuel cell) and amount of pure H_2 produced.

(Eq. (20)), the reformer shows excellent ability to provide a large output of extra-pure H_2, even when its operation is limited by insufficient membrane area or permeability. This H_2 can be used for electricity generation using fuel cells, but also for ultraclean combustion gas turbines and as a chemical feedstock. The remaining (unseparated) fraction of fuel which, after condensation, contains unreacted CH_4, unseparated H_2, and a significant amount of CO can be used for electricity generation using gas turbines as well as for other applications after post-treatment.

The pure H_2 production rate and normalized to power output cost of Pd are plotted in right panel of Fig. 12. Based on this prediction, the reformer cost should be reasonable, especially for high reformer throughputs. For low space velocities, there is a sharp increase in H_2 production with increasing reformer throughput. As the reformer throughput is further increased, its performance becomes limited by the membrane separation ability; note that the maximal attained value of $Q(H_2)$ is in good agreement with the maximal H_2 flux of the membrane which parameters were used for simulations ($E_{H_2} = 11$ kJ/mol, $A_{H_2} = 5.6$ mol/(m^2 s bar$^{0.5}$)) (Patrascu and Sheintuch, 2015). To sum up, the reformer is expected to provide excellent performance with a reasonable capital cost investment, but complete assessment of economic feasibility should include other system components and should be supported by experimental proof-of-concept.

5. Concluding remarks

A medium-scale solar molten salt-heated membrane reformer was analyzed numerically using computational fluid dynamics in a specific temperature range relevant to the use of solar parabolic troughs. The results of numerical simulations show that the efficiency of the solar heat supply by a molten salt flow and the membrane separation ability are crucial for the reformer performance. Strong temperature and concentration gradients were observed for high reformer throughputs. Despite these transport limitations, the reformer shows overall good performance even at elevated space velocities.

For moderate throughputs, i.e. space velocities below 10,000 h^{-1}, the reformer demonstrates excellent performance in terms of methane conversion and hydrogen recovery. For space velocities below 5000 h^{-1}, the reformer provides nearly complete methane conversion and hydrogen recovery of as high as 90%. At the same time, a power density of ca. 2 kW/L and a fuel heating value upgrade of ca. 40% are achieved. A preliminary techno-economic evaluation shows reasonable capital cost investment and good performance even for elevated, industrially relevant reformer throughputs. It is important to note at the end, that the simulation results shown herein still need to be experimentally evaluated, addressing challenges related to membrane durability, catalyst activity, and to effective system-level integration of the membrane reformer.

Acknowledgements

The authors acknowledge the support of King Fahd University of Petroleum and Minerals through the research grant # R12-CE-10 offered by the KFUPM-MIT Clean Water and Clean Energy Research Collaboration Center.

References

Agrafiotis, C., Storch, H.v., Roeb, M., Sattler, C., 2014. Solar thermal reforming of methane feedstocks for hydrogen and syngas production – a review. Renew. Sust. Energy Rev. 29, 656–682.

Angeli, S.D., Monteleone, G., Giaconia, A., Lemonidou, A.A., 2014. State-of-the-art catalysts for CH_4 steam reforming at low temperature. Int. J. Hydrogen Energy 39, 1979–1997.

Armor, J.N., 1999. The multiple roles for catalysis in the production of H_2. Appl. Catal. A 176, 159–176.

Balat, M., 2008. Potential importance of hydrogen as a future solution to environmental and transportation problems. Int. J. Hydrogen Energy 33, 4013–4029.

Chibane, L., Djellouli, B., 2011. Methane steam reforming reaction behaviour in a packed bed membrane reactor. Int. J. Chem. Eng. Appl. 2, 147–156.

Coroneo, M., Montante, G., Baschetti, M.G., Paglianti, A., 2009. CFD modelling of inorganic membrane modules for gas mixture separation. Chem. Eng. Sci. 64, 1085–1094.

Coroneo, M., Montante, G., Paglianti, A., 2010. Numerical and experimental fluid-dynamic analysis to improve the mass transfer performances of Pd–Ag membrane modules for hydrogen purification. Ind. Eng. Chem. Res. 49, 9300–9309.

Crabtree, G.W., Dresselhaus, M.S., Buchanan, M.V., 2004. The hydrogen economy. Phys. Today 57, 39–45.

Ewan, B.C.R., Allen, R.W.K., 2005. A figure of merit assessment of the routes to hydrogen. Int. J. Hydrogen Energy 30, 809–819.

Falco, M.D., Piemonte, V., 2011. Solar enriched methane production by steam reforming process: reactor design. Int. J. Hydrogen Energy 36, 7759–7762.

Falco, M.D., Paola, L.D., Marrelli, L., Nardella, P., 2007. Simulation of large-scale membrane reformers by a two-dimensional model. Chem. Eng. J. 28, 115–125.

Falco, M.D., Giaconia, A., Marrelli, L., Tarquini, P., Grena, R., Caputo, G., 2009. Enriched methane production using solar energy: an assessment of plant performance. Int. J. Hydrogen Energy 34, 98–109.

Fernandes, F.A.N., Soares Jr., A.B., 2006. Methane steam reforming modeling in a palladium membrane reactor. Fuel 85, 569–573.

FLUENT User's guide. In: Fluent Inc. <http://www.fluent.com>.

Giaconia, A., Falco, M.d., Caputo, G., Grena, R., Tarquini, P., Marrelli, L., 2008. Solar steam reforming of natural gas for hydrogen production using molten salt heat carriers. AIChE J. 54, 1932–1944.

Giaconia, A., Turchetti, L., Monteleone, G., Morico, B., Iaquaniello, G., Shabtai, K., et al., 2013. Development of a solar-powered fuel-flexible compact steam reformer: the CoMETHy Project. Chem. Eng. Trans. 35, 433–438.

Goto, S., Assabumrungrat, S., Tagawa, T., Praserthdam, P., 2000. The effect of direction of hydrogen permeation on the rate through a composite palladium membrane. J. Membr. Sci. 175, 19–24.

Holladay, J.D., Hu, J., King, D.L., Wang, Y., 2009. An overview of hydrogen production technologies. Catal. Today 139, 244–260.

Holleck, G.L., 1970. Diffusion and solubility of hydrogen in palladium and palladium-silver alloys. Phys. Chem. 74, 503–511.

Hou, K., Hughes, R., 2001. The kinetics of methane steam reforming over a Ni/a-Al_2O_3 catalyst. Chem. Eng. J. 82, 311–328.

Joensen, F., Rostrup-Nielsen, J.R., 2002. Conversion of hydrocarbons and alcohols for fuel cells. J. Power Sources 105, 195–201.

Kearney, D., Herrmann, U., Nava, P., Kelly, B., Mahoney, R., Pacheco, J., et al., 2003. Assessment of a molten salt heat transfer fluid in a parabolic trough solar field. J. Solar Energy Eng. 125, 170–176.

Keller, C.F., Warming, Global., 2007. An update to global warming: the balance of evidence and its policy implications. Sci. World J. 7 (2007), 381–399.

Kyriakides, A.-S., Ipsakis, D., Voutetakis, S., Papadopoulou, S., Seferlis, P., 2013. Modelling and simulation of a membrane reactor for the low temperature methane steam reforming. Chem. Eng. Trans. 35, 109–114.

Patrascu, M., Sheintuch, M., 2015. On-site pure hydrogen production by methane steam reforming in high flux membrane reactor: experimental validation, model predictions and membrane inhibition. Chem. Eng. J. 262, 862–874.

Piatkowski, N., Wieckert, C., Weimer, A.W., Steinfeld, A., 2011. Solar-driven gasification of carbonaceous feedstock – a review. Energy Environ. Sci. 4, 73–82.

Rodríguez, M.L., Pedernera, M.N., Borio, D.O., 2012. Two dimensional modeling of a membrane reactor for ATR of methane. Catal. Today 193, 137–144.

Romero, M., Steinfeld, A., 2012. Concentrating solar thermal power and thermochemical fuels. Energy Environ. Sci. 5, 9234–9245.

Said, S.A.M., Simakov, D.S.A., Mokheimer, E.M.A., Habib, M.A., Ahmed, S., Waseeuddin, M., Román-Leshkov, Y., 2015. Computational fluid dynamics study of hydrogen generation by low temperature methane reforming in a membrane reactor. Int. J. Hydrogen Energy 40, 3158–3169.

Sheintuch, M., Simakov, D.S.A., 2011. Alkanes dehydrogenation. In: Falco, M.D., Marrelli, L., Iaquaniello, G. (Eds.), Membrane Reactors for Hydrogen Production Processes. Springer-Verlag, London Limited, New York, pp. 183–200.

Simakov, D.S.A., Sheintuch, M., 2008. Design of a thermally balanced membrane reformer for hydrogen production. AIChE J. 54, 2735–2750.

Simakov, D.S.A., Sheintuch, M., 2009. Demonstration of a scaled-down autothermal membrane methane reformer for hydrogen generation. Int. J. Hydrogen Energy 34, 8866–8876.

Simakov, D.S.A., Sheintuch, M., 2010. Experimental optimization of an autonomous scaled-down methane membrane reformer for hydrogen Generation. Ind. Eng. Chem. Res. 49, 1123–1129.

Simakov, D.S.A., Sheintuch, M., 2011. Model-based optimization of hydrogen generation by methane steam reforming in autothermal packed-bed membrane reformer. AIChE J. 57, 525–541.

Simakov, D.S.A., Wright, M.M., Ahmed, S., Mokheimerd, E.M.A., Román-Leshkov, Y., 2015. Solar thermal catalytic reforming of natural gas: a review on chemistry, catalysis and system design. Catal. Sci. Technol. 5, 1991–2016.

Steinfeld, A., 2005. Solar thermochemical production of hydrogen – a review. Solar Energy 78, 603–615.

Uemiya, S., Sato, N., Ando, H., Matsuda, T., Kikuchi, E., 1991. Steam reforming of methane in a hydrogen-permeable membrane reactor. Appl. Catal. 67, 223–230.

Xu, J., Froment, G.F., 1989a. Methane steam reforming: II. Diffusional limitations and reactor simulation. AIChE J. 35, 97–103.

Xu, J., Froment, G.F., 1989b. Methane steam reforming, methanation and water-gas shift: 1. Intrinsic kinetics. AIChE J. 35, 88–96.

Younglove, B.A., 1982. Thermophysical properties of fluids part I. J. Phys. Chem. Ref. Data. 11 (Suppl. 1), 4–7.

Younglove, B.A., Ely, J.F., 1987. Thermophysical properties of fluids. Part II. J. Phys. Chem. Ref. Data 16, 577.

Yun, S., Oyama, S.T., 2011. Correlations in palladium membranes for hydrogen separation: a review. J. Membr. Sci. 375, 28–45.